Human Ecology
Online ISSN: 3041-9255
www.landscapeecologyjournals.ir

ORIGINAL ARTICLE
Vol. 5, Special Issue 1 (2026) | Article e247132
DOI: https://doi.org/10.22034/he.2026.589654.1242
Received: 2 Jul 2026 | Accepted: 13 Jul 2026
Published: 28 Nov 2026

Article DOI

Modeling Land Surface Temperature at a Local Scale Using a Machine Learning Algorithm and Analysis of Spectral Indices and Air Quality Parameters During the Lockdown Period, Before and After

Amir Arsalan Ghafouri*

School of Surveying and Geospatial Engineering, College of Engineering, University of Tehran, Tehran, Iran.

*** Corresponding author:** Amir Arsalan Ghafouri; amirarsalanghafoori@gmail.com

ORCID: 0009-0009-5577-615X

Abstract

The SARS-CoV-2 (COVID-19) outbreak poses a serious threat to humans, society, and the global economy. Strict global control measures to limit virus spread have several positive environmental consequences. The study offers an unprecedented opportunity to understand and quantify human impacts on the atmospheric environment. New York City has seen a decrease in average LST and a negative rate of change in this key parameter (-0.83% in NYC). The LST was validated against air temperature measured at meteorological stations across NYC (RMSE = 6.34 °C and R^2 = 0.94). Meanwhile, the quarantine plans reduced concentrations of NO_2, SO_2, O_3, and CO. The rate of change of these parameters during the quarantine period was negative and included (NO_2 (-30.0%), O_3 (-31.25%), (0) SO_2, and CO (-25%)). During the lockdown, fewer moving vehicles and people on the roads reduced pollution and directly improved the urban environment. This study compares the environmental status of the index (NDVI), NDBI, NDWI, and Albedo during the lockdown period in NYC with pre-lockdown (2015-2019) and post-lockdown (2021) periods. The results show that the NDVI and NDWI have a positive change rate during the lockdown period, respectively; the rates of change of these two during the lockdown period are (0.45 %, 2.29%), and the range of changes during this period was negative in the case of the NDBI index (-0.85%). Finally, this study aims to model LST at the local scale using an Artificial Neural Network (ANN). Therefore, land surface spectral indices (land cover indices) and air quality parameters can be used as indices that affect LST. We investigated the relationship between six spectral indices, air quality parameters, and LST, and used the indices most strongly correlated with LST as neural network inputs. Because the correlation results with LST differed by period, the neural network inputs also differed by period. In the pre-lockdown period, the input parameters included (NDBI, Albedo, CO, and NDWI); during lockdown, (NDWI, NDBI, SO2, and NO2); and post-lockdown, (NDBI, Albedo, CO, and NDWI). The ANN model provided accurate results in training and testing, with (RMSE) and (R2) values, respectively, in all three periods (RMSE: 0.004, R2: 0.71), (RMSE: 0.003, R2: 0.73), (RMSE: 0.003, R2: 0.72).

Keywords: Artificial Neural Network; Air Quality; COVID-19; Land Surface Temperature

1. Introduction

Coronavirus disease (COVID-19) is a communicable disease caused by the coronavirus SARS-CoV-2 (Islam et al., 2021). The disease was first reported in Wuhan, China, on December 31, 2019, and spread quickly worldwide due to its contagious nature, raising concern globally (Qin et al., 2020). COVID-19 has been declared the latest "Public Health Emergency of International Concern (PHEIC)" by the World Health Organization (WHO). Over a hundred countries have implemented strict nationwide containment measures (lockdowns) in response to the health emergency. COVID-19 is expected to arrive in the United States in early January 2020. The first confirmed COVID-19 case of native transmission in the United States was discovered on January 15, 2020, in Washington state, and COVID-19 spread rapidly throughout the country. California, New York, Florida, Louisiana, North Carolina, and Alabama were the states with the highest number of cases and deaths in the United States. Finally, in North America, government-mandated home confinement lasted during the lockdowns (March-May 2020) (Parida et al., 2021).

Lockdown procedures reduce air pollution and create a society with lower environmental pollution (Bashir et al., 2020; Chakraborty & Maity, 2020; Garg, Aggarwal, and Chauhan, 2020; Gupta, Raghuwanshi, and Chanda, 2020). As a result, reduced transportation and industrial activity lower pollution levels. Some researchers report a link between UHI and pollution caused by a combination of turbulent and radiative transfer processes, emphasizing the importance of studying these elements concurrently (Di Sabatino et al., 2020; Schaefer et al., 2021). Furthermore, this lockdown's immediate positive environmental impact was evident in reduced air temperature and land surface temperature (LST) (Shi et al., 2020; Yunus, Masago, and Hijioka, 2020).

Despite studies that conclusively link environmental pollution to increased LST and, thus, UHI intensity (Schwarz, Lautenbach, and Seppelt, 2011; Li et al., 2011; Logan et al., 2020). LST has decreased by 0.13 °C in Osaka (Nakajima et al., 2021); 0.49 °C in Tokyo (Fujibe, 2020); 1 °C in Montreal (Canada) (Teufel et al., 2021); and 3 to 5 °C in the Dwarka River basin (Mandal & Pal, 2020), with values ranging from 5 to 8 °C in the San Francisco Bay area (Potter & Alexander, 2021). In addition, a study of Mumbai, Delhi, Kolkata, and Chennai (India) reports a 19.2 percent decrease in average UHI intensity during the lockdown period (Ghosh et al., 2020).

Greenhouse gases like CO, NO2, and SO_2 are thought to be the primary cause of climate change and disease. Studying their concentrations is critical in extreme conditions like COVID-19. These gases, however, also influence changes in LST. (García and Díaz 2022). The confinement and extreme measures in terms of social distancing, transportation restrictions, industrial production, and human activities have resulted in unprecedented temporary decreases in aerosols and air pollutants (NO_2, CO, SO_2, and PM), owing primarily to the restriction of fossil fuel burning and sclerotic traffic exhaust (Marinello, Butturi, and Gamberini 2021; Muhammad, Long, and Salman 2020) Several studies have found significant reductions in air pollutants in urban areas all over the world as a result of national lockdowns (Bauwens et al., 2020; Wang & Su, 2020; Bao & Zhang, 2020) NO2 concentration has dropped by 20–30%, or even more, in urban centers of China (Bao & Zhang, 2020), India (Mahato, Pal, and Ghosh 2020), Malaysia (Abdullah et al. 2020), Brazil (Nakada & Urban, 2020), and the USA. Depending on lockdown effectiveness, cities in Europe and the United States with full lockdowns reportedly showed larger reductions in NO2 concentrations (18-40%), while cities with no or partial lockdowns showed no significant reduction in NO2 concentration (3-7.5%) (Bar et al., 2021). In addition to reducing environmental pollution and land surface temperature, lockdowns also affected biophysical indices (Ghosh et al., 2020).

According to these studies, the negative environmental impacts of these activities were significantly reduced due to the complete cessation of the industrial, transportation, and tourism sectors, as well as a significant reduction in population congestion in public spaces during the COVID-19 confinement. This study considered eleven elements: LST, NDVI, NDWI, IBI, BD, CO, NO_2, SO_2, O_3, and NDBI. Although NDVI, NDWI, IBI, BD, and NDBI are more or less stable in nature, these parameters may change slightly due to the imposition of the lockdown phenomenon, aside from the undisturbed

condition of the natural environment; above all, these parameters are very important for assessing environmental quality (Liang & Weng, 2010; Akbari, Rosenfeld, and Taha, 1990; Li & Weng, 2007; Ghosh et al., 2020). Recent studies, for example, used Earth observation data to show the impact of the COVID-19 lockdown on environmental conditions. The results show that the COVID-19 year (2020) had the highest native vegetation cover at 28.5 percent, despite having the lowest rainfall of the three years (93 mm), compared to 6 percent in 2017 and 2 percent in 2018 (Al-Ali et al., 2021). In addition, the emergence of new vegetation in previously open spaces in selected Indian cities results in a high level of greenery during this period. This pattern applies to all megacities, which is a good sign for environmental health. The normalized differential water index (NDWI) is another indicator of environmental health. NDWI patterns in the study areas range from -0.55 to 0.32 for Mumbai, -0.55 to 0.54 for Delhi, -0.56 to 0.31 for Kolkata, and -0.53 to 32 for Chennai, indicating that moisture levels in the study areas are not particularly high at any time during the study (Ghosh et al., 2020).

This research traces the effect of the COVID-19 pandemic on changes in the physical environment using satellite-image-derived Air Quality (AQ) and Spectral Indices (SI) and modeling LST for the pre-lockdown, lockdown, and post-lockdown periods in NYC.

The overarching goals of this study are to (1) analyze changes in LST in the previous period (2019), during lockdown (March 2020), and after that (2020), using both satellite and ground-based station measurements, and (2) analyze changes in air quality parameters during lockdown, before, and after that. (3) Examine changes in SI over three time periods. Finally, we modeled LST using Machine Learning (ML) techniques, such as the ANN algorithm, with AQ indices and SI before, during, and after the COVID-19 pandemic in NYC.

2. Materials and methods

2.1. Study area and data source

New York City (NYC) is the largest city in the United States, with an estimated 2019 population of over 836,800 residents (United States Census Bureau, 2016), covering ~740 km2, and a median altitude of 10 m. Located within the jap a part of the continental United States, NYC is split into 5 122 boroughs (Brooklyn, The Bronx, Queens, Staten Island, and Manhattan) of various sizes, 123 populations, and socioeconomic classes (1).

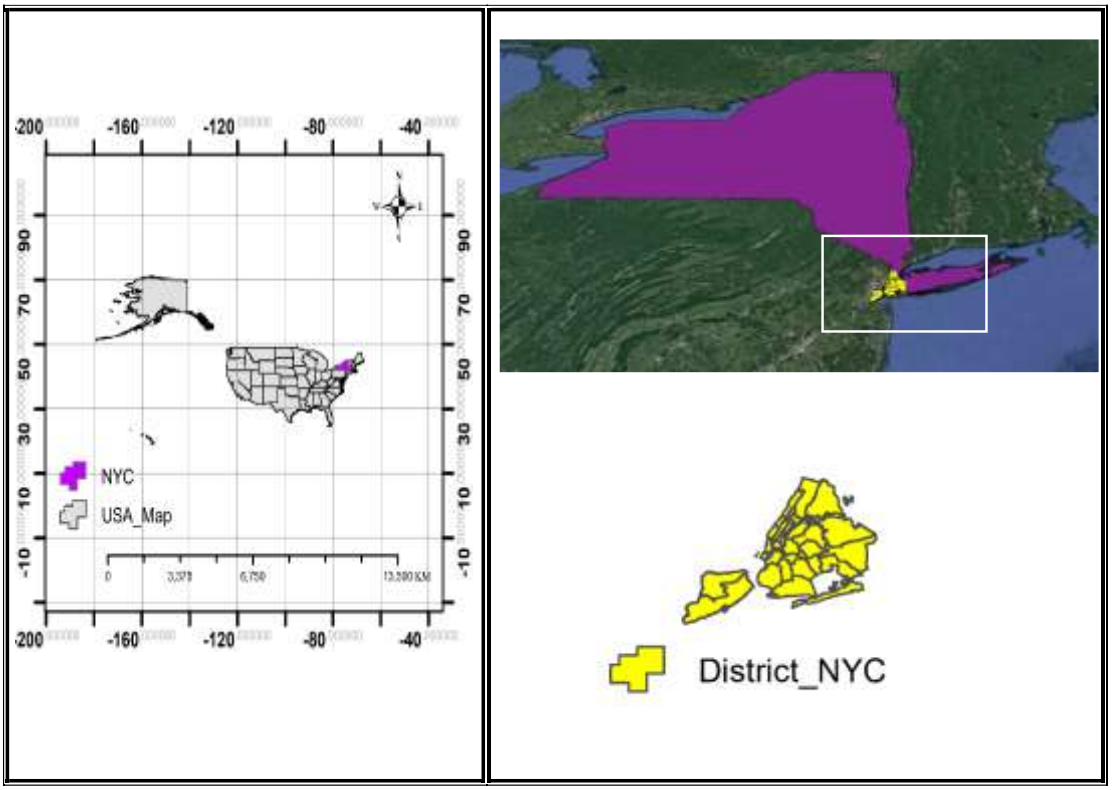


Fig. 1. Study area (NYC)

Satellite-derived measurements of LST, SI, and AQ provide a comprehensive estimate of lockdown impacts on LST across NYC. Table 1 summarizes the datasets used in this study, which are described in the following sections.

Table 1. Datasets used in the study

Data used	Resolution	Source
Land Surface Temperature(Landsat-8, TIRS)	Spatial: 30m	https://code.earthengine.google.com/
Spectrall Indices(Landsat-8, OLI)	Spatial: 30m	https://code.earthengine.google.com/
Air Quality(Sentinel-5)	Spatial: 3.5 x 7 km	https://code.earthengine.google.com/
Ground station: Air temperature variables	Location (NYC)	https://www.visualcrossing.com/weather/weather-data-services

2.2. Spectral indices

The spectral indices of vegetation, urban surface cover, and water surface cover are used to identify changes. Vegetation is directly related to moisture, heat, and radiation and influences surface temperature (Weng, Lu, and Schubring 2004; Sarli et al., 2026). NDVI is a green vegetation index that reflects the separation between vegetation, water, and soil (Brovkin, 2002; Yuan & Bauer, 2007). Because of the internal structure of plant leaves, they reflect more in the infrared spectrum and absorb more in the red spectrum. According to Equation 1, these two bands are used to calculate NDVI. NDVI values range from -1 to -1.

$$NDVI = \frac{\rho_{NIR} - \rho_{RED}}{\rho_{NIR} + \rho_{RED}} \quad (1)$$

NDBI indicates impenetrable urban areas, shows the extent of urban areas, and is an important analytical tool for describing land development, urbanization, and Land Surface parameters (Ranagalage et al., 2018; Dai, Guldmann, and Hu, 2018; Morabito et al., 2016). When reflection in the short infrared spectrum exceeds reflection in the infrared spectrum, it indicates built-up areas and bare ground. The NDBI index is calculated using Equation 2, and its value ranges from -1 to 1.

$$NDBI = \frac{\rho_{SWIR} - \rho_{NIR}}{\rho_{SWIR} + \rho_{NIR}} \quad (2)$$

NDWI indicates water coverage and land moisture content (McFeeters, 1996; Lasaponara & Masini, 2012). The NDWI index is used to analyze water bodies. The NDWI parameter is calculated using Equation 3, and its value ranges from -1 to 1.

$$NDWI = \frac{\rho_G - \rho_{NIR}}{\rho_G + \rho_{NIR}} \quad (3)$$

In this study, for albedo computation, Landsat 8 bands 2, 4, 5, 6, and 7 were downloaded and converted from TIFF to .img format so the digital numbers could be identified (DN). Using Equation, the converted Landsat bands were then converted to radiance (4) (Naegeli et al., 2017; Odunuga & Badru, 2015).

$$L_{\lambda=(Gain_\lambda * D_n)+Bias_\lambda} \quad (4)$$

where L_λ = radiance (in watts/(sq. meter × μm × ster); Gain = (Lmax – Lmin)/255; Bias = Lmin; and Dn = Digital Number of the Landsat band.

The obtained radiance values for the bands were further processed to obtain the at-surface reflectance (R_λ) for the bands using Equation (5).

$$R_\lambda = \frac{\pi * L_\lambda * d_2}{Esun,\lambda * \sin(\theta SE)} \quad (5)$$

where R_λ = at surface reflectance; π = 3.142; L_λ = radiance calculated with formula (1); d = earth-sun distance; Esun, λ = band-specific radiance emitted by the sun; θSE = Sun elevation angle.

Small negative reflectance errors were introduced when converting the Landsat band from radiance to reflectance. These are not physical and must be corrected. The reflectance errors were corrected using Equation (6)

$$R_{\lambda c} = CON([reflectance] < 0.0, 0.0, [reflectance]) \quad (6)$$

The corrected reflectance for bands 2, 4, 5, 6, and 7 was then utilized in Equation (7) to calculate the albedo (α) (Liang, 2001).

$$\alpha \frac{0.35\alpha_2 + 0.13\alpha_4 + 0.373\alpha_5 + 0.085\alpha_6 + 0.072\alpha_7 - 0.0018}{1.016} \quad (7)$$

2.3. Land surface temperature

To estimate LST, we used the single-channel algorithm (Ru et al., 2021; Yu, Guo, and Wu, 2014; Windahl & de Beurs, 2016; Duan et al., 2019; Kamali Maskooni et al., 2021) for summer images from 2000 to 2019. We calculate surface temperature using cloud-free satellite imagery and suitable atmospheric conditions. Equation 8 shows how to calculate the LST.

$$LST = \frac{B_T}{\left(1 + \left((\lambda * B_T)/\rho\right) * Ln(LSE)\right)} \quad (8)$$

In Equation 1, the value of $\rho = \frac{hc}{K}\left(1.438 * 10^{-2}\, mK\right)$ in which λ is the emitted wavelength (m), h is the Planck constant, and K is the Boltzmann constant. The two parameters,B_T Moreover, LSE is the land surface emissivity. From formula 9, the brightness temperature can be calculated.

$$B_T = \frac{K_2}{L_n\left(\frac{K_1}{L_\lambda} + 1\right)} \quad (9)$$

In Equation 2, B_T is the effective brightness temperature in Kelvin, and L_λ is the spectral radiance of the sensor in units of $(w/(m^2.sr.\mu m))$ and the values K_1 and K_2 are the constants for the first and second calibrations (wm^{-2}), where images from different Landsat satellite series differ in the image header file. The values K_1 and K_2 for TM, ETM +, and TIRS sensors are presented in Table 2.

Table 2. Calibration constants for Landsat satellite series

Sensors	K_1	K_2
TM	607.76	1260.56
ETM+	666.09	1282.71
TIRS	774.88	1321.07

The amount of energy a real object emits at a given temperature and wavelength, relative to the amount of energy a complete black body emits at the same temperature and wavelength, is called the object's emission coefficient. When calculating the temperature of a land surface using satellite imagery, accurately estimating the surface's emissivity is important. In contrast, an incorrect emissivity estimate, or ignoring it, can increase temperature-calculation error by up to 1 or 2 degrees Kelvin (Caselles et al., 1995). Surface emissivity depends on parameters such as properties, water content, chemical composition, physical structure, and texture (Snyder et al., 1998). Surface emissivity also varies across wavelengths. In areas with dense land cover, assuming a constant emission coefficient is reasonable. However, in areas with little vegetation or bare land with different soil and mineral types, you must consider each pixel's emissivity. When measuring temperature. In the absence of the necessary facilities for laboratory testing, satellite images are used to calculate the emissivity of different materials and ground characteristics at different wavelengths. NDVI is one of the most common methods (Valor & Caselles, 1996). In the present study, we used the NDVI-based method presented by Van de Griend (1993) to estimate emissivity. We calculated average emissivities for wasteland, green space, forest parks, water bodies, asphalt surfaces, and residential areas as 0.932, 0.937, 0.937, 0.931, 0.933, and 0.932, respectively. We estimate land surface propagation using the NDVI threshold method (Duan et al., 2019; Kamali Maskooni et al., 2021; Yu, Guo, and Wu, 2014). Table 3 lists the emissivity calculation formulas for Landsat 5, 7, and 8.

Table 3. Diffusion formula for images of Landsat 5, 7, and 8

Landsat 8	Landsat 7,5
$LSE = \varepsilon_S (1 - FVC) + (\varepsilon_V FVC)$	$LSE = (0.004 * P_V) + 0.986$
$\varepsilon_S = 0.97$, $\varepsilon_V = 0.99$ Obtained from the ASTER spectral library.(Tardy et al. 2016; Jiménez-Muñoz et al. 2008; Carlson, Perry, and Schmugge 1990).	$P_V = \left(\frac{NDVI - NDVI_{min}}{NDVI_{max} - NDVI_{min}} \right)^2$

The Fractional Vegetation Cover (FVC) is calculated using Equation 10.

$$FVC = \frac{NDVI - NDVI_S}{NDVI_V - NDVI_S} \quad (10)$$

In Equation 6, $NDVI_s$ and $NDVI_v$ are vegetation classifications for soil and vegetation property classification, respectively.

2.4. Satellite data validation

Satellite-derived values require verification (Sarli et al., 2025). In recent decades, comparing LST values with ambient temperatures has become an increasingly important validation method (Srivastava, Majumdar, and Bhattacharya, 2009; Gallo et al., 2011; Mukherjee & Singh, 2020; García & Díaz, 2021). We compare the recovered LST with ambient temperature measured by weather

stations. In this study, we validated LSTs from Landsat 8 satellite images against station environmental temperature values during satellite passage.

(https://www.visualcrossing.com/weather/weather-data-services)(García and Díaz 2022).

2.5. Air quality

Researchers examined the spatiotemporal distribution of air pollutants such as NO2, SO2, CO, and O3 before, during, and after the COVID-19 pandemic lockdown using satellite imagery collections. We used TROPOMI daily data to create maps of monthly spatial patterns of air pollutants. Offline level 3 tropospheric NO2 vertical column density (COPERNICUS/S5P/OFFL/L3 NO_2), offline level 3 ground level SO_2 vertical column density (COPERNICUS/S5P/OFFL/L3 SO_2), offline level 3 ground level SO_2 vertical column density (COPERNICUS/S5P/OFFL/L3 CO), offline level 3 ground level CO vertical column density, and (COPERNICUS/S5P/OFFL/L3 O_3) offline level 3 ground level O_3 vertical column density. It also tracks the different effects of atmospheric gases across the electromagnetic spectrum. The sensor operates in the transverse direction and has a ground swath width of 2600 km. Except for the SWIR and UV bands, which are 7 7 km^2 and 7 28 km^2, the nadir view for all spectral bands is 7 3.5 km^2. (Ghasempour, Sekertekin, and Kutoglu 2021). In this study, however, all Sentinel-5P-derived products have a spatial resolution of 0.01 arc degrees (1.111 km) in GEE.

2.6. Rate of change (concentration)

Understanding the changes in concentrations of air quality parameters, physical parameters, and LST before and after the lockdown period is critical. After retrieving data on pollutants, physical parameters, and land surface temperature, we classified the spatial and temporal patterns of the parameters' average levels into three groups. (i) before lockdown (March and May 2015-2019); (ii) during lockdown (March and May 2020); and (iii) after lockdown (March and May 2021). (March and May 2021). We calculated the rate of change using Eq. (11) (Alqasemi et al., 2021). This reflects the percentage change in the levels of the desired parameters in the study area before and after the lockdown (i.e., 2015-2019), and it is also compared with the length of the lockdown in 2020.

$$\text{Change rate (\%)} = \left(\frac{X_{2019}-X_{2015}}{X_{2015}}\right)*100$$

$$\text{Change rate (\%)} = \left(\frac{X_{2020}-X_{2019}}{X_{2019}}\right)*100$$

$$\text{Change rate (\%)} = \left(\frac{X_{2021}-X_{2020}}{X_{20120}}\right)*100 \quad (11)$$

2.7. Artificial neural networks

To find the best linear regression equation, this study developed an approach using artificial neural networks. In this manner, after receiving the input data (features), the neural network creates an output layer using input and hidden layers. The neural network used the ReLU (Rectified Linear Unit) activation function to obtain the values of the weights of the middle neurons (hidden layer). In the output layer, however, a linear function was used to achieve the desired result. In addition, after reviewing the structure of the previously mentioned neural network, at least 15 neurons were considered for the middle (hidden) layer (in order to optimize the model with the lowest complexity of the network structure) (Figure 2)

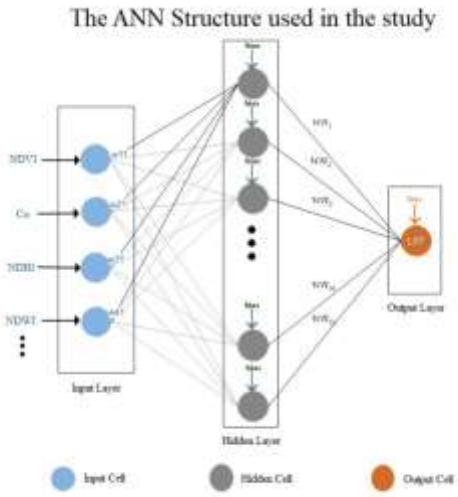


Fig. 2. ANN structure

Figure 3 illustrates the schematic diagram of the proposed method.

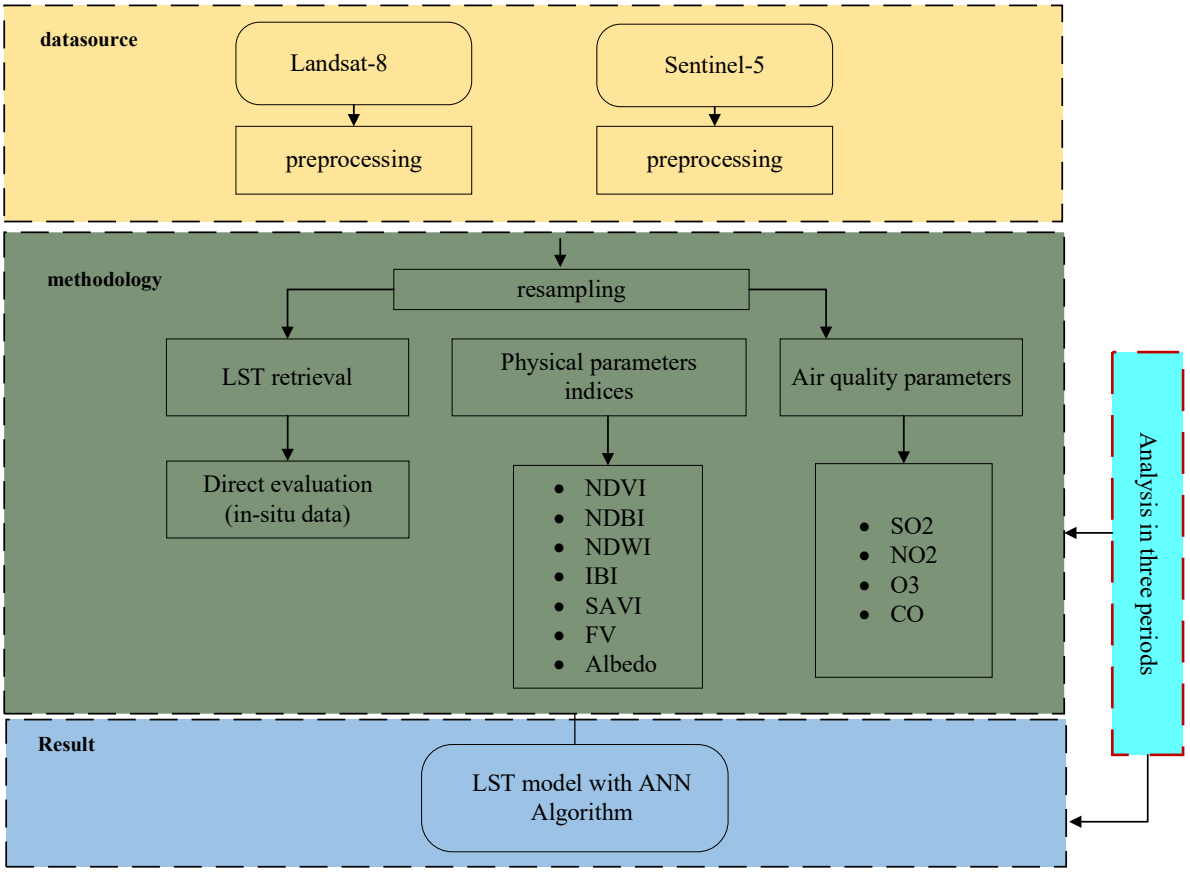


Fig. 3. Implementation process

3. Results and discussion

3.1. Land surface temperature analysis in three periods (before, during, and after lockdown)

To validate the satellite data, we calculated the linear regression coefficients and R2 between the LST obtained with Landsat 8 and the ambient temperatures acquired from https://www.visualcrossing.com/weather/weather-data-services. The root mean squared error (RMSE) for the Landsat 8 dataset was 6.34 °C, and R2 was 0.94. These values indicate a good agreement between the analyzed values.

The average LST values in March and May images (2015–2019) were higher than the average LST values in the locked images of March and May (2020). This trend increased after the lockdown period (2021) (Table 4. The average LST in March and May images during the lockdown period is (18.90 °C, 21.88 °C), compared to the years before lockdown (2015-2019) (11.01 °C, 28.34°C, 12.41°C, 26.17°C, 9.63°C, 22.01°C, 10.93°C, 12.41°C, 33.09°C), which has been steadily increasing over time. On the other hand, the graph of the rate of change in Figure 4 shows that in the years before lockdown, the rate of change in the average LST was positive and increasing (5.40%), while during the lockdown, the results show that the average LST was decreasing, and its rate of change was (-0.83%). Similarly, in the post-lockdown period, the rate of change in the binomial was positive and increasing (1.05%). Overall, the results show a positive change during the lockdown phase. This is mainly due to lower population density and different vehicle types on the roads. Reduced transportation and industrial pollutants played an important role in lowering the average LST during the quarantine period in NYC. The Landsat-8 LST results are similar to those of other studies (Nanda, Mishra, and Swain 2021; Mukherjee & Debnath, 2020; Saputra et al., 2022; Alqasemi et al., 2021; Parida et al., 2021; García & Díaz, 2022).

The LST results reported here indicate significant reductions in house arrest periods compared to non-incarceration periods in 2015–2019 and 2021, results supported by statistical analysis. Taken together, these conditions suggest that closures of the tourism, industry, and transportation sectors due to confinement significantly improve surface temperatures.

Table 4. Descriptive statistics of LST

Date	Cloud cover (%)	Min	Max	Mean	St.D
2015-03-12	3.67	-2.44	21.12	11.01	2.47
2015-05-22	4.05	4.28	45.16	28.34	3.69
2016-03-21	6.5	-7.57	25.96	12.41	3.53
2016-05-08	8.8	2.53	45.9	26.17	3.37
2017-03-17	1.54	-1.67	23.65	9.63	1.29
2017-05-04	4.38	-2.44	41.12	22.01	2.51
2018-03-11	8.28	-4.55	25.59	10.93	2.12
2019-03-07	22.02	3.26	29.81	12.41	3.73
2019-05-20	18.36	7.26	45.92	33.09	3.84
2020-03-09	0.36	-7.26	20.54	8.90	2.85
2020-05-12	2.55	-2.46	35.37	21.88	3.20
2021-03-03	13.28	0.97	23.96	10.72	2.10
2021-05-15	7.8	14.28	49.81	30.83	4.37

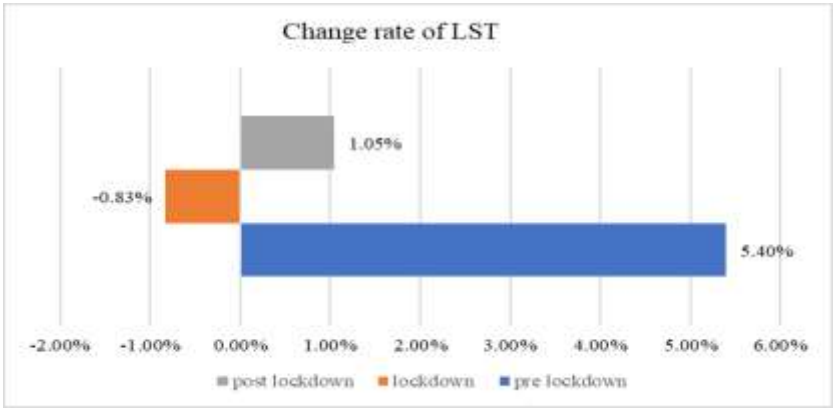


Fig. 4. Change rate of LST

3.2. Physical parameter indices analysis

Environmental quality has deteriorated in recent decades due to population growth and increased human intervention in the natural environment. Environmental physical parameters such as air quality, water quality, land surface temperature, and many others have changed rapidly overall. The lockdown showed positive signs of recovery from environmental degradation, with physical parameters improving (Mahato, Pal, and Ghosh 2020). Furthermore, reduced anthropogenic heat flux in the near-surface atmosphere lowered LST, helping mitigate the natural increase from the previous year (Muhammad, Long, and Salman 2020). Not only these two parameters, but also biophysical parameters such as NDVI, NDWI, NDBI, and Albedo have changed due to the uninterrupted or undisturbed conditions of the natural environment (Ghosh et al., 2020).

Table 5 shows the average NDVI for April and May from 2015 to 2021. The lockdown steps had a relatively large effect on NDVI. During the quarantine stage, average NDVI values were higher than in the preceding and following periods. Lower pollution and vegetation health unaffected by human disturbances (emissions, traffic, industrial activities, etc.) indicate higher NDVI. Figure 5 shows that the NDVI change rate before lockdown decreased (-0.41 %), whereas the vegetation change rate during lockdown increased (0.45 %) and remained high in the post-lockdown period (0.47 %). This is a positive sign for the lockdown period; however, new vegetation in previously open spaces leads to a high level of greenery during this time. This study shows that human activities affect an area's vegetation. NDVI results show that vegetation increased during the lockdown period. These findings show that lockdown reduces the negative effects of human activity. Because rainfall was low during this time, regional vegetation can recover quickly during drought seasons as long as the disturbance source is kept to a minimum. (Guha and Govil 2021; Al-Ali et al. 2021). At broader spatial scales, researchers have also examined heat–drought exposure across forest and cropland ecosystems using multiple climatic indicators and CMIP6 projections (Sarli & Marapao, 2027).

Table 5. Descriptive statistics of NDVI

Date	Cloud cover (%)	Min	Max	Mean	St.D
2015-03-12	3.67	-0.98	0.97	0.08	0.14
2015-05-22	4.05	-0.89	0.97	0.31	0.24
2016-03-21	6.5	-0.97	0.90	0.13	0.18
2016-05-08	31.8	-0.52	0.91	0.18	0.18
2017-03-17	1.54	-1	0.98	-0.05	0.12
2017-05-04	4.38	-1	0.96	0.27	0.22
2018-03-11	8.28	-1	1	0.12	0.20
2019-03-07	22.02	-1	0.93	0.11	0.19
2019-05-20	18.36	-0.99	1	0.32	0.27
2020-03-09	0.36	-1	1	0.15	0.20
2020-05-12	2.55	-0.99	0.98	0.27	0.24
2021-03-03	13.28	-1	1	0.12	0.18
2021-05-15	7.8	-1	0.99	0.29	0.27

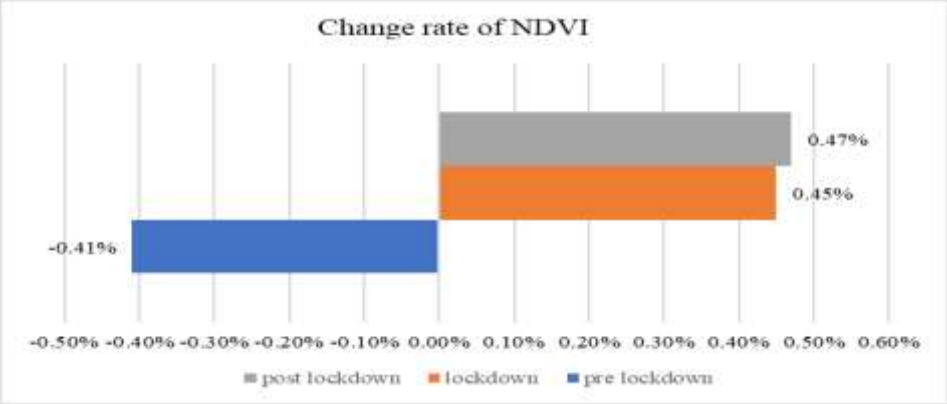


Fig. 5. Change rate of NDVI

The average NDWI in the study areas varies (0.03, 0.08, 0.05, 0.9, 0.58, 0.07, -0.04, -0.03, 0.07) during the lockdown (0.16, 0.11) and after the lockdown (-0.03, 0.1) for NYC from 2015 to 2019, indicating that the amount of humidity in the study is variable (Table 6). According to the range-of-changes diagram in Figure 6, the range of changes in water bodies and surface humidity in the pre-lockdown period is (-4.20%), while the range of changes in average NDWI during the lockdown is around (2.29%) and post-lockdown is around (3.50%). Overall, NDWI values in NYC increased during the lockdown period compared with the pre-lockdown and post-lockdown years (2015-2019). Some published studies also reported a positive change in this index during the lockdown period (Ghosh et al., 2020; Liang & Weng, 2010).

Table 6. Descriptive statistics of NDWI

Date	Cloud cover (%)	Min	Max	Mean	St.D
2015-03-12	3.67	-0.98	1	0.03	0.16
2015-05-22	4.05	-0.66	0.72	0.08	0.13
2016-03-21	6.5	-0.89	0.97	0.05	0.09
2016-05-08	31.8	-0.74	0.73	0.09	0.11
2017-03-17	1.54	-1	1	0.58	0.17
2017-05-04	4.38	-0.72	0.80	0.07	0.11
2018-03-11	8.28	-1	1	0.03	0.15
2019-03-07	22.02	-1	1	0.16	0.20
2019-05-20	18.36	-0.96	0.94	0.11	0.14
2020-03-09	0.36	-1	1	0.09	0.11
2020-05-12	2.55	-0.97	0.88	0.17	0.12
2021-03-03	13.28	-1	1	0.03	0.11
2021-05-15	7.8	-0.94	1	0.1	0.13

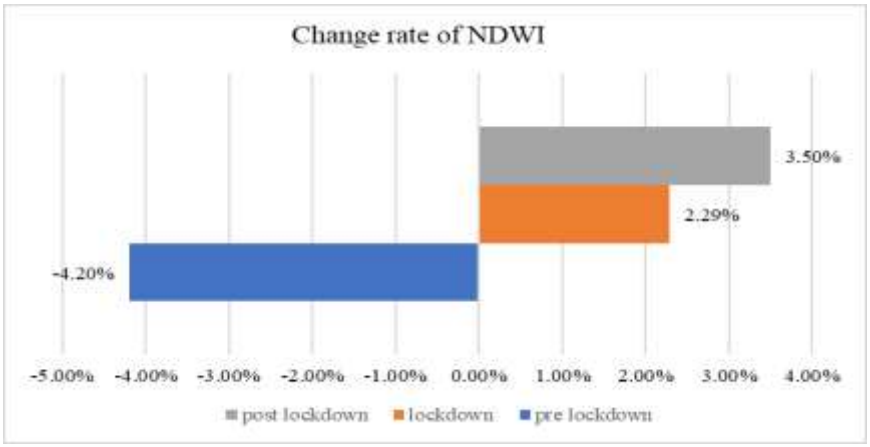


Fig. 6. Change rate of NDWI

Statistical Table 7 shows the average NDBI index for April and May in the pre-quarantine period. The trend is relatively stable, but during the quarantine period, the average changed to (5.62, 1.05) and showed a decreasing trend. According to Figure 7, the range of changes decreased by about (-0.83%) during the lockdown period and increased by about (1.05%) in the post-lock period.

Table 7. Descriptive statistics of NDBI

Date	Cloud cover (%)	Min	Max	Mean	St.D
2015-03-12	3.67	-1	1	-0.04	0.16
2015-05-22	4.05	-0.72	0.72	-0.09	0.13
2016-03-21	6.5	-0.97	0.97	-0.01	0.09
2016-05-08	31.8	-0.74	0.73	-0.09	0.11
2017-03-17	1.54	-1	1	-0.59	0.17
2017-05-04	4.38	-1	0.80	-0.08	0.11
2018-03-11	8.28	-0.8	1	-0.02	0.15
2019-03-07	22.02	-1	1	-0.021	0.21
2019-05-20	18.36	-0.95	0.96	-0.08	0.14
2020-03-09	0.36	-1	1	-0.17	0.11
2020-05-12	2.55	-0.88	0.97	-0.11	0.12
2021-03-03	13.28	-1	1	0.027	0.11
2021-05-15	7.8	-1	0.94	-0.11	0.13

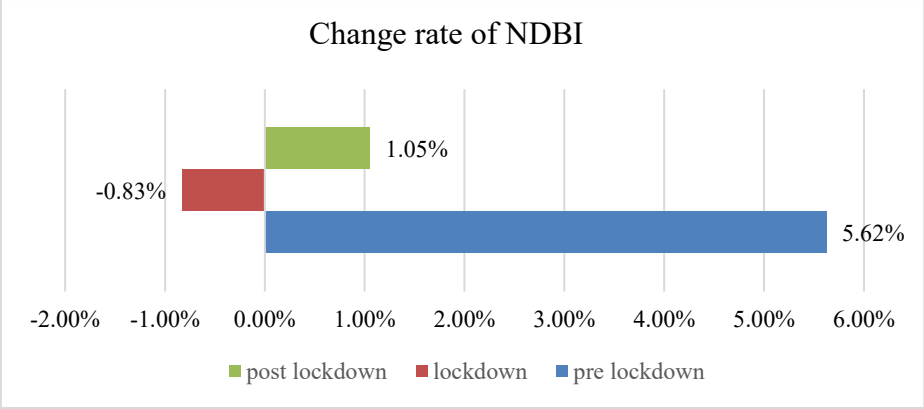


Fig. 7. Change rate of NDBI

3.3. Albedo change analysis

Albedo calculations in pre-lockdown years ranged between 0.1 and 0.19, whereas during the lockdown (0.09, 0.13) and in the post-lockdown period (0.09, 0.14). In the pre-lock period, albedo followed a trend similar to LST, increasing absorption and decreasing reflection of incoming solar radiation, the opposite of the lock period's downward trend. Table 8 below presents the statistical results for albedo.

Table 8. Descriptive statistics of albedo

Date	Cloud cover (%)	Min	Max	Mean	St.D
2015-03-12	3.67	-0.027	0.97	0.1	0.04
2015-05-22	4.05	-0.017	1.30	0.13	0.05
2016-03-21	6.5	-0.009	1.23	0.09	0.04
2016-05-08	31.8	0.008	0.82	0.18	0.12
2017-03-17	1.54	-0.05	0.74	0.25	0.1
2018-03-11	8.28	-0.07	1.43	0.05	0.12
2019-03-07	22.02	-0.06	1.43	0.09	0.05
2019-05-20	18.36	-0.06	1.15	0.19	0.21
2020-03-09	0.36	-0.05	0.71	0.09	0.08
2020-05-12	2.55	0	0.95	0.13	0. 04
2021-03-03	13.28	-0.01	1.12	0.09	0.04
2021-05-15	7.8	0	1.35	0.14	0.04

In contrast, Figure 8 shows that the albedo change rate is negative during the lockdown period, whereas it is positive before and after the lockdown.

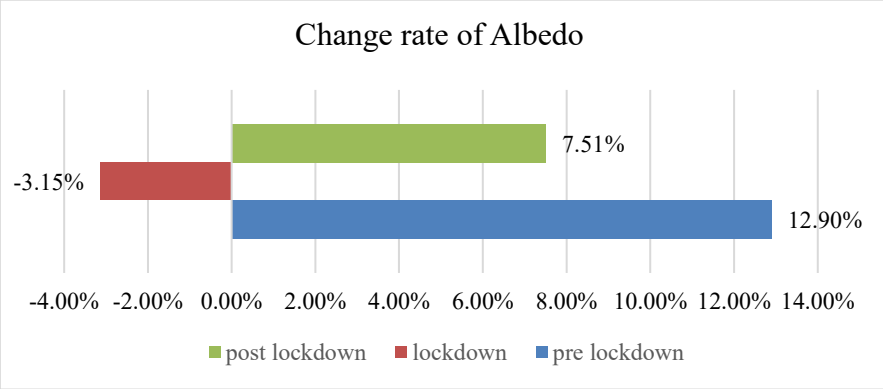


Fig. 8. Change rate of albedo

3.4. Air quality parameter indices analysis

During the COVID-19 lockdown in NYC (2020), air quality parameter concentrations decreased significantly. The average values of the considered daily air pollutants (SO_2, NO_2, CO, O_3) in NYC decreased significantly compared with the average values from 2015 to 2019 and the same period in 2020, and this downward trend continued in 2021. It rose after the lockdown, when restrictions were lifted (Tables 9, 10, 11, 12). The average reduction of the analyzed parameters was as follows: NO_2 (-30.0%), O3 (-31.25%), (0) So2, and CO (-25%). On the other hand, in the post-lockdown era, NYC saw an increase in air quality parameters; i.e., in 2021, the increase in the average values of these results included NO_2 (20 %), O_3 (54.25%), CO (26 %), and SO_2 (33.33 %), respectively. These findings support the importance of transportation and industry in driving high pollution levels in cities. Figure 9 shows the average daily decreases in the variables studied. The analysis shows that NO2, SO2, O3, and CO levels in NYC decreased because of limited transportation and factory closures. This finding is consistent with previous research conducted in various parts of the world (Baldasano, 2020; Dantas et al., 2020; Islam et al., 2021; Alqasemi et al., 2021).

The Covid-19 pandemic caused a large number of infections and deaths in the United States of America (Hopkins, 2021). To limit the spread of the coronavirus, the United States implemented strict

control measures, primarily from March to May 2020, including partial to total quarantine of industrial production and citizen movement (Parida et al., 2021). As a result, lockdown measures reduced air pollution. During the lockdown, atmospheric pollution (NO_2, SO_2, CO, O_3) decreased across NYC, mirroring the city's global decline (Cadotte, 2020; Dutheil, Baker, and Navel, 2020). Lockdown measures not only reduced infection prevalence in the most affected countries, but also improved the overall environment and reduced mortality (Mahato, Pal, and Ghosh, 2020; Tobías et al., 2020). It has been reduced early in some Chinese cities (Wang & Su, 2020). In Europe, approximately 2,190 premature deaths (2,420-1,960) have been avoided, with a projected reduction of 13,600 to 29,500 depending on quarantine effectiveness (Giani et al., 2020). In 2020, an estimated 0.78 (0.09-1.5) million premature deaths are expected to be avoided globally (Venter et al., 2020).

Table 9. Descriptive statistics of NO_2

Date	Cloud cover (%)	Min	Max	Mean	St.D
2019-03-07	22.02	0.01	0.03	0.03	0.003
2019-05-20	18.36	0.01	0.02	0.03	0.003
2020-03-09	0.36	0	0.01	0.01	0.002
2020-05-12	2.55	0	0.02	0.02	0.002
2021-03-03	13.28	0.01	0.05	0.05	0.002
2021-05-15	7.8	0.01	0.06	0.06	0.001

Table 10. Descriptive statistics of SO_2

Date	Cloud cover (%)	Min	Max	Mean	St.D
2019-03-07	22.02	-0.07	0.02	0.03	0.006
2019-05-20	18.36	-0.07	0.02	0.03	0.006
2020-03-09	0.36	-0.09	0.01	0.03	0.005
2020-05-12	2.55	-0.09	0.01	0.02	0.005
2021-03-03	13.28	-0.09	0.03	0.03	0.009
2021-05-15	7.8	-0.09	0.03	0.04	0.004

Table 11. Descriptive statistics of CO

Date	Cloud cover (%)	Min	Max	Mean	St.D
2019-03-07	22.02	0.038	0.043	0.04	0.001
2019-05-20	18.36	0.036	0.042	0.04	0.001
2020-03-09	0.36	0.035	0.043	0.03	0.001
2020-05-12	2.55	0.032	0.040	0.036	0.002
2021-03-03	13.28	0.035	0.041	0.038	0.001
2021-05-15	7.8	0.034	0.045	0.039	0.002

Table 12. Descriptive statistics of O_3

Date	Cloud cover (%)	Min	Max	Mean	St.D
2019-03-07	22.02	0.16	0.17	0.16	0.005
2019-05-20	18.36	0.17	0.18	0.18	0.008
2020-03-09	0.36	0.11	0.13	0.11	0.001
2020-05-12	2.55	0.13	0.14	0.13	0.007
2021-03-03	13.28	0.16	0.17	0.17	0.001
2021-05-15	7.8	0.16	0.17	0.16	0.001



Fig. 9. Change rate of air quality parameters

3.5. The relationship between LST, spectral indices and air quality parameters

In this first section, we investigate the relationship between LST and spectral indices to determine which indices correlate more strongly with LST. Thus, we used only the highly correlated indices in the ANN instead of all indices. This procedure reduces the number of ANN inputs and enables high-accuracy results with minimal inputs. The second section presents the ANN architecture by illustrating the inputs and the number of hidden layers. The third section presents the ANN mathematical model and the LST maps of the study area obtained using this ANN model (Sekertekin, Arslan, and Bilgili 2020).

Figure 10 shows the selected pair plots showing the relationships among the spectral indices, air quality parameters, and LST. After reviewing the pair plots, we determined which indices correlated more strongly with LST. Therefore, we used the selected indices as neural network inputs, and the selected indicators differed by year: pre-lockdown, during lockdown, and post-lockdown. Because air quality parameter data were available from late 2018, we evaluated only spectral index data from 2015. The pair plots showed that until 2019 (pre-lockdown), spectral indices had an almost constant effect on LST, including NDBI, Albedo, CO, and NDWI. However, during the lockdown, the effects of these indices changed slightly; the influential indices and parameters included (NDWI, NDBI, SO2, and NO2), and the post-lockdown results showed (NDBI, CO, NDVI, and Albedo).

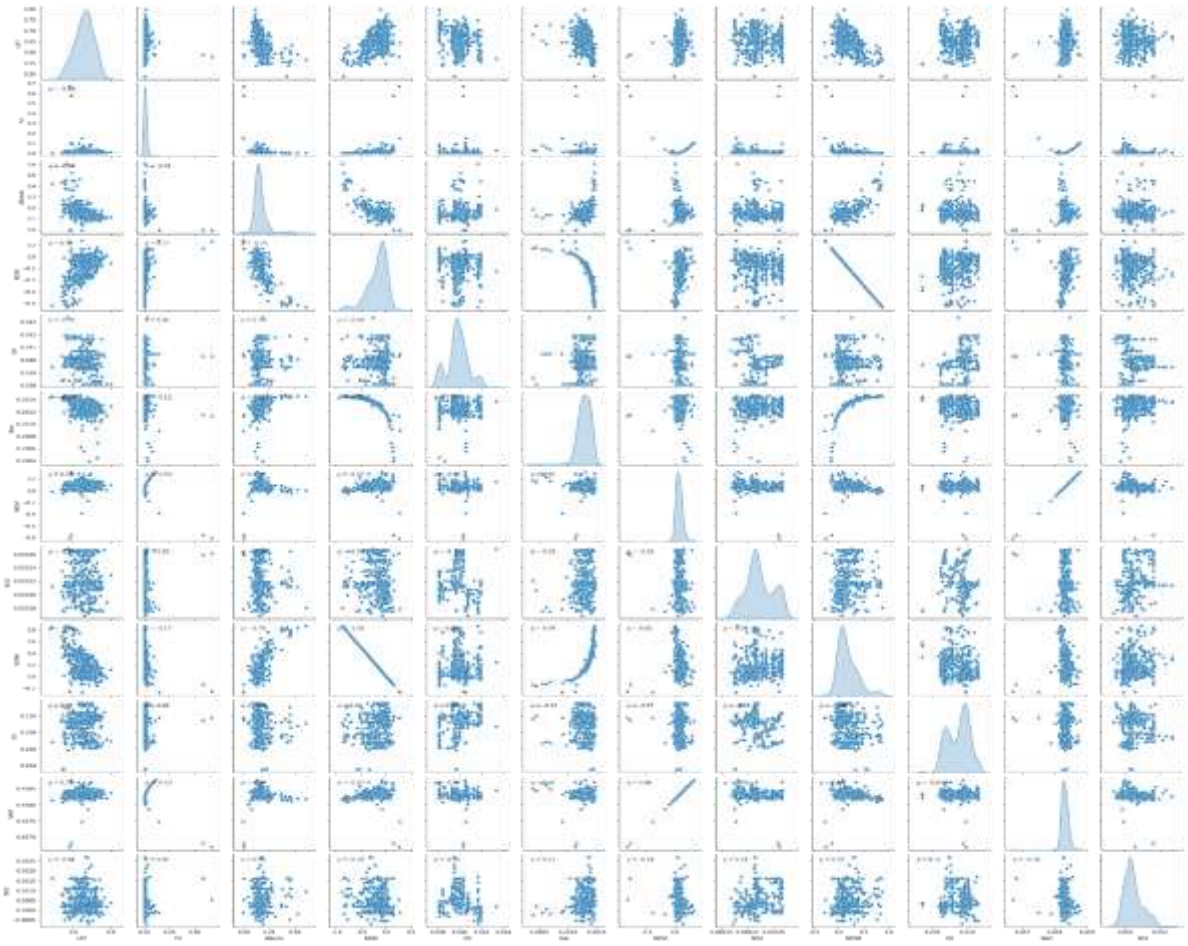


Fig. 10. Pair plot of relationship between the spectral indices and air quality parameters with the LST (2019-03-07)

3.6. ANN algorithm and results

This study is the first to model LST based on several spectral remote sensing indices and air quality parameters across three periods: pre-lockdown, during the lockdown, and after. Previous studies were considered to investigate the correlation between LST and a limited number of spectral indices and air quality parameters in the pre-lockdown and the during the lockdown (García & Díaz, 2022; Nanda, Mishra, and Swain, 2021; Mukherjee & Debnath, 2020; Alqasemi et al., 2021; Parida et al., 2021).

TIR-based LST algorithms require atmospheric parameters (air temperature, relative humidity, water vapor content, and atmospheric transport), surface parameters (LSE and LSG), and sensor parameters (spectral resolution and viewing angle). When compared to TIR remote sensing, the main advantages of the ANN method in LST retrieval are I less input selection, (ii) satellite-based input variables can be obtained from different satellites, and (iii) no need for complex statistical processes between variables. However, one disadvantage of ANN-based LST modeling over TIR-based LST modeling is that if the ANN's input data are site-dependent (global or continental), the model may differ in other regions and may not function properly. However, the results were good (Sekertekin, Arslan, and Bilgili 2020). In this study, the ANN method modeled LST at a local scale in NYC. The results showed that the effect of air quality indices and parameters on LST differs across the three periods; therefore, the algorithm inputs differ by period based on each index's influence. Figure 11 presents the time series and scatter plots of the optimal ANN model for the training and testing datasets. As shown in Figure 11, the ANN represented the data well in each period, with (RMSE: 0.004, R2: 0.71), (RMSE: 0.003, R2: 0.73), and (RMSE: 0.003, R2: 0.72), and provided satisfactory results.

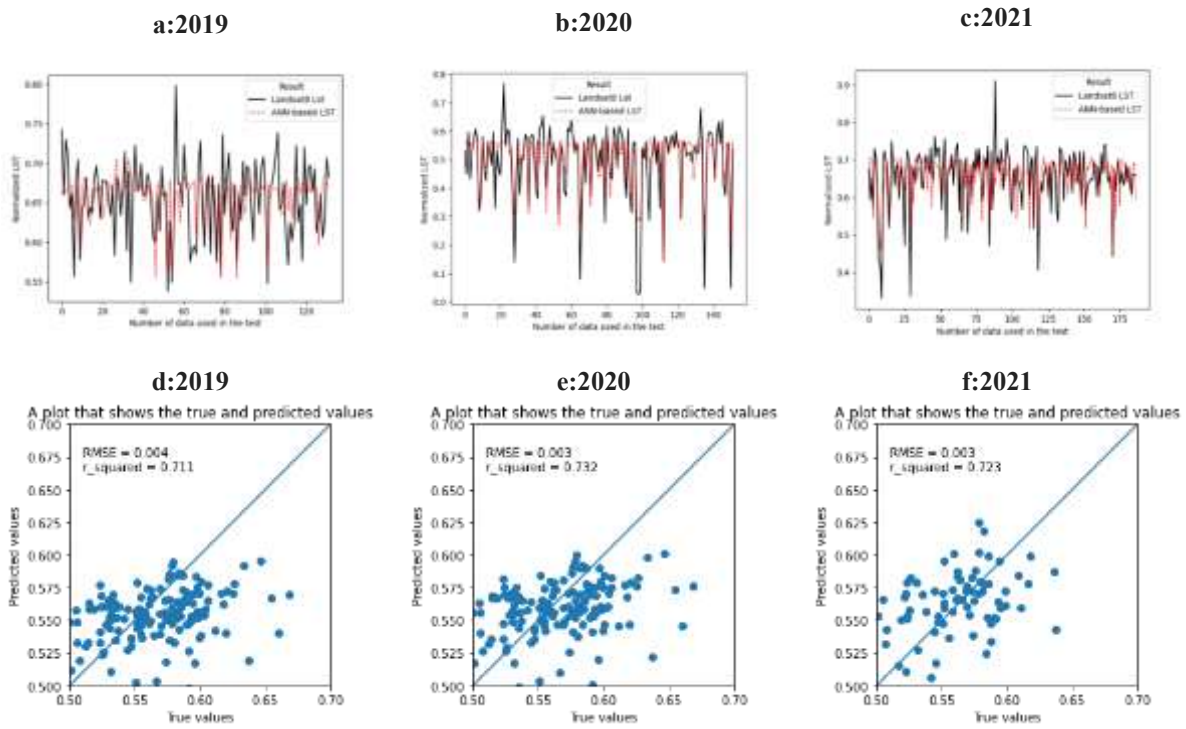


Fig. 11. ANN results for testing data sets: (a–c) time series of testing data over three periods; (d–f) regression plots for testing data over three periods.

4. Conclusions

This research included several scenarios:

- Evaluation of LST over three periods (pre-lockdown, lockdown, and post-lockdown)
- Air quality parameters were evaluated over three time periods (pre-lockdown, lockdown, and post-lockdown)
- Spectral indices were evaluated across all three time periods (pre-lockdown, lockdown, and post-lockdown)

The parameters and indices influencing changes in the LST were chosen based on their correlation with the LST over all three time periods (pre-lockdown, lockdown, and post-lockdown)

Important indices and parameters were chosen as neural network inputs to model the LST over all three time periods (pre-lockdown, lockdown, and post-lockdown)

Because of massive reductions in human activities such as transportation, industrial production, and energy consumption, the COVID-19 pandemic has caused a temporary improvement in global air quality.

The current study's findings indicate a general downward trend in LST, air quality parameters, and biophysical parameters such as the NDBI index in NYC during the lockdown period (March and May) of the epidemic year (2020), compared with the same periods in 2015–19. During the lockdown, average indices such as NDVI and NDWI also increased in NYC. The decrease in the temperature of the earth's surface in NYC during the lockdown period was observed that the average LST from 2015 to 2019 had an almost increasing trend, which included (11.01 °C, 28.34°C, 12.41°C, 26.17°C, 9.63°C, 22.01°C, 10.93°C, 12.41°C, 33.09°C) but in the lockdown period are (8.9°C, 21.88°C) and in post-lockdown are (10.72°C, 30.83°C) in all three periods before, lock periods, and after, respectively, while during the locking period the average LST had almost negative growth and the range of changes in the average LST reached an all-time low (-0.83%). The current study found that NO2, SO2, O3, and CO concentrations decreased throughout NYC during the pandemic lockdown, as predicted, with rates of change of NO2 (-30.0%), O3 (-31.25%), SO2 (0), and CO (-25%). Finally, in line with the study's

objectives, we identified the parameters and indices that most strongly influenced changes in LST and selected them as neural network inputs. Because the index and influencing parameters differed slightly in each period, we selected the neural network inputs accordingly. The result was three LSTM models in the three periods: the lockdown, pre-lockdown, and post-lockdown periods, with RMSE and R^2 (RMSE:0.004, R^2: 071), (RMSE:0.003, R^2: 073), (RMSE:0.003, R^2: 072).

Overall, the study found that overall environmental quality in NYC improved compared to the previous year (same months), though given the overall trend of environmental quality degradation, 2020 should have the worst environmental conditions compared to the previous year. Have a wonderful and safe 2019. This study aimed to understand environmental conditions and model LST across all three periods based on these conditions.

References

Abdullah, S.; A.A. Mansor; N.N.L.M. Napi; W.N.W. Mansor; A.N. Ahmed; M. Ismail; and Z.T.A. Ramly. 2020. Air quality status during 2020 Malaysia Movement Control Order (MCO) due to 2019 novel coronavirus (2019-nCoV) pandemic. *Science of The Total Environment* **729:139022**.

Akbari, H.; A.H. Rosenfeld; and H. Taha. 1990. Summer heat islands, urban trees, and white surfaces.

Al-Ali, Z.M.; M.M. Abdullah; A.A. Assi; M.S. Alhumimidi; A.-Q.S. Wasan; and T.S. Ali. 2021. The immediate impact of the associated COVID-19 lockdown campaign on the native vegetation recovery of Wadi Al Batin Tri-state desert. *Remote Sensing Applications: Society and Environment* **23:100557**.

Alqasemi, A.S.; M.E. Hereher; G. Kaplan; A.M.F. Al-Quraishi; and H. Saibi. 2021. Impact of COVID-19 lockdown upon the air quality and surface urban heat island intensity over the United Arab Emirates. *Science of The Total Environment* **767:144330**.

Baldasano, J.M. (2020). COVID-19 lockdown effects on air quality by NO2 in the cities of Barcelona and Madrid (Spain). *Science of The Total Environment,* **741:140353**.

Bao, R. & A. Zhang. (2020). Does lockdown reduce air pollution? Evidence from 44 cities in northern China. *Science of The Total Environment* **731:139052**.

Bar, S.; B.R. Parida; S.P. Mandal; A.C. Pandey; N. Kumar; and B. Mishra. 2021. Impacts of partial to complete COVID-19 lockdown on NO2 and PM2. 5 levels in major urban cities of Europe and the USA. *Cities* **117:103308**.

Bashir, M.F.; B. Ma; B. Komal; M.A. Bashir; D. Tan; and M. Bashir. 2020. Correlation between climate indicators and the COVID-19 pandemic in New York, USA. *Science of The Total Environment* **728:138835**.

Bauwens, M.; S. Compernolle; T. Stavrakou; J.F. Müller; J. Van Gent; H. Eskes; P.F. Levelt; R. Van Der A; J. Veefkind; and J. Vlietinck. 2020. Impact of coronavirus outbreak on NO2 pollution assessed using TROPOMI and OMI observations. *Geophysical Research Letters* **47:e2020GL087978**.

Brovkin, V. (2002). Climate-vegetation interaction. In *Journal de Physique IV (Proceedings)*, 57–72: EDP Sciences.

Cadotte, M. (2020). Early evidence that COVID-19 government policies reduce urban air pollution.

Carlson, T.N.; E.M. Perry; and T.J. Schmugge. 1990. Remote estimation of soil moisture availability and fractional vegetation cover for agricultural fields. *Agricultural and Forest Meteorology* **52:45-69**.

Caselles, V.; C. Coll; E. Valor; and E. Rubio. 1995. Mapping land surface emissivity using AVHRR data application to La Mancha, Spain. *Remote Sensing Reviews* **12:311-333**.

Chakraborty, I. & P. Maity. (2020). COVID-19 outbreak: Migration, effects on society, global environment and prevention. *Science of The Total Environment* **728:138882**.

Dai, Z.; J.-M. Guldmann; and Y. Hu. 2018. Spatial regression models of park and land-use impacts on the urban heat island in central Beijing. *Science of the Total Environment* **626:1136-1147**.

Dantas, G.; Siciliano, B.; França, B.B.; da Silva, C.M.; and Arbilla, G. 2020. The impact of COVID-19 partial lockdown on the air quality of the city of Rio de Janeiro, Brazil. *Science of The Total Environment* **729:139085**.

Di Sabatino, S.; F. Barbano; E. Brattich; and B. Pulvirenti. 2020. The multiple-scale nature of urban heat island and its footprint on air quality in a real urban environment, *Atmosphere* **11:1186**.

Duan, S.-B.; Z.-L. Li; C. Wang; S. Zhang; B.-H. Tang; P. Leng; and M.-F. Gao. 2019. Land-surface temperature retrieval from Landsat 8 single-channel thermal infrared data in combination with NCEP reanalysis data and ASTER GED product. *International Journal of Remote Sensing* **40:1763-1778**.

Dutheil, F.; J.S. Baker; and V. Navel. 2020. COVID-19 as a factor influencing air pollution? *Environmental Pollution* **263:114466**.

Fujibe, F. (2020). Temperature anomaly in the Tokyo metropolitan area during the COVID-19 (coronavirus) self-restraint period. *SOLA*.

Gallo, K.; R. Hale; D. Tarpley; and Y. Yu. 2011. Evaluation of the relationship between air and land surface temperature under clear-and cloudy-sky conditions, Journal *of Applied Meteorology and Climatology* **50:767-775**.

García, D.H., & Díaz, J. A. (2021). Modeling of the Urban Heat Island on local climatic zones of a city using Sentinel 3 images: Urban determining factors. *Urban Climate* **37:100840**.

García DH, Díaz JA. (2021). Impacts of the COVID-19 confinement on air quality, the Land Surface Temperature and the urban heat island in eight cities of Andalusia (Spain). *Remote Sensing Applications: Society and Environment*, 25: 100667. https://doi.org/10.1016/j.rsase.2021.100667.

Garg, V.; S.P. Aggarwal; and P. Chauhan. 2020. Changes in turbidity along Ganga River using Sentinel-2 satellite data during lockdown associated with COVID-19: Geomatics*, Natural Hazards and Risk* **11:1175-1195**.

Ghasempour, F.; A. Sekertekin; and S.H. Kutoglu. 2021. Google Earth Engine-based spatio-temporal analysis of air pollutants before and during the first wave COVID-19 outbreak over Turkey via remote sensing, *Journal of Cleaner Production* **319:128599**.

Ghosh, S.; A. Das; T.K. Hembram; S. Saha; B. Pradhan; and A.M. Alamri. 2020. Impact of COVID-19-induced lockdown on environmental quality in four indian megacities using Landsat 8 OLI and TIRS-derived data and Mamdani fuzzy logic modeling approach. *Sustainability* **12:5464**.

Guha, S. & H. Govil. (2021). COVID-19 lockdown effect on land surface temperature and normalized difference vegetation index. *Geomatics, Natural Hazards and Risk* **12:1082-1100**.

Gupta, S.; G.S. Raghuwanshi; and A. Chanda. 2020. Effect of weather on COVID-19 spread in the US: A prediction model for India in 2020, *Science of the Total Environment* **728:138860**.

Hopkins, J. (2021). New cases of COVID-19 in world countries.

Islam, M.S.; T.R. Tusher; S. Roy; and M. Rahman. 2021. Impacts of nationwide lockdown due to COVID-19 outbreak on air quality in Bangladesh: a spatiotemporal analysis. *Air Quality, Atmosphere & Health* **14:351-363**.

Jiménez-Muñoz, J.C.; J. Cristóbal; J.A. Sobrino; G. Sòria; M. Ninyerola; and X. Pons. 2008. Revision of the single-channel algorithm for land surface temperature retrieval from Landsat thermal-infrared data. *IEEE Transactions on Geoscience and Remote Sensing* **47:339-349**.

Kamali Maskooni, E.; H. Hashemi; R. Berndtsson; P. Daneshkar Arasteh; and M. Kazemi. 2021. Impact of spatiotemporal land-use and land-cover changes on surface urban heat islands in a semiarid region using Landsat data, *International Journal of Digital Earth* **14:250-270**.

Lasaponara, R. & N. Masini. (2012). *Satellite remote sensing: A new tool for archaeology*. Springer Science & Business Media.

Li, G. & Q. Weng. (2007). Measuring the quality of life in city of Indianapolis by integration of remote sensing and census data. *International Journal of Remote Sensing* **28:249-267**.

Li, J.; C. Song; L. Cao; F. Zhu; X. Meng; and J. Wu. 2011. Impacts of landscape structure on surface urban heat islands: A case study of Shanghai, China. *Remote Sensing of Environment* **115:3249-3263**.

Liang, B. & Q. Weng. (2010). Assessing urban environmental quality change of Indianapolis, United States, by the remote sensing and GIS integration. *IEEE Journal of Selected Topics in Applied Earth Observations and Remote Sensing* **4:43-55**.

Liang, S. (2001). Narrowband to broadband conversions of land surface albedo I: Algorithms. *Remote sensing of environment* **76:213-238**.

Logan, T.; B. Zaitchik; S. Guikema; and A. Nisbet. 2020. Night and day: The influence and relative importance of urban characteristics on remotely sensed land surface temperature. *Remote Sensing of Environment* **247:111861**.

Mahato, S.; S. Pal; and K.G. Ghosh. 2020. Effect of lockdown amid COVID-19 pandemic on air quality of the megacity Delhi, India. *Science of The Total Environment* **730:139086**.

Marinello, S.; M.A. Butturi; and R. Gamberini. 2021. How changes in human activities during the lockdown impacted air quality parameters: A review. *Environmental progress & sustainable energy* **40:e13672**.

McFeeters, S.K. (1996). The use of the Normalized Difference Water Index (NDWI) in the delineation of open water features. *International Journal of Remote Sensing,* **17:1425-1432**.

Morabito, M.; Crisci, A.; Messeri, A.; Orlandini, S.; Raschi, A.; Maracchi, G.; and Munafò, M. 2016. The impact of built-up surfaces on land surface temperatures in Italian urban areas. *Science of the Total Environment* **551:317-326**.

Muhammad, S.; X. Long; and M. Salman. 2020. COVID-19 pandemic and environmental pollution: A blessing in disguise? *Science of The Total Environment* **728:138820**.

Mukherjee, F. & D. Singh. (2020). Assessing land use–land cover change and its impact on land surface temperature using LANDSAT data: A comparison of two urban areas in India. *Earth Systems and Environment* **4:385-407**.

Mukherjee, S. & A. Debnath. (2020). Correlation between land surface temperature and urban heat Island with COVID-19 in New Delhi, India.

Naegeli, K.; A. Damm; M. Huss; H. Wulf; M. Schaepman; and M. Hoelzle. 2017. Cross-comparison of albedo products for glacier surfaces derived from airborne and satellite (Sentinel-2 and Landsat 8) optical data. *Remote Sensing* **9:110**.

Nakada, L.Y.K. & R.C. Urban. (2020). COVID-19 pandemic: Impacts on the air quality during the partial lockdown in São Paulo state, Brazil. *Science of The Total Environment* **730:139087**.

Nanda, D.; D.R. Mishra; and D. Swain. 2021. COVID-19 lockdowns induced land surface temperature variability in mega urban agglomerations in India. *Environmental Science: Processes & Impacts* **23:144-159**.

Odunuga, S. & G. Badru. (2015). Land cover change, land surface temperature, surface albedo and topography in the Plateau Region of North-Central Nigeria. *Land* **4:300-324**.

Parida, B.R.; S. Bar; D. Kaskaoutis; A.C. Pandey; S.D. Polade; and S. Goswami. 2021. Impact of COVID-19-induced lockdown on land surface temperature, aerosol, and urban heat in Europe and North America: Sustainable *Cities and Society* **75:103336**.

Potter, C. & O. Alexander. (2021). Impacts of the San Francisco Bay Area shelter-in-place during the COVID-19 pandemic on urban heat fluxes. *Urban Climate* **37:100828**.

Qin, C.; M.P.L.Z.M. Ziwei; S.Y.M.Y. Tao; P.C.X.M.P. Ke; and M.M.P.K. Shang. 2020. Dysregulation of immune response in patients with COVID-19 in Wuhan, China; Clinical Infectious Diseases; Oxford Academic. *Clinical Infectious Diseases*.

Ranagalage, M.; R.C. Estoque; X. Zhang; and Y. Murayama. 2018. Spatial changes of urban heat island formation in the Colombo District, Sri Lanka: Implications for sustainability planning. *Sustainability* **10:1367**.

Ru, C.; S.-B. Duan; X.-G. Jiang; Z.-L. Li; Y. Jiang; H. Ren; P. Leng; and M. Gao. 2021. Land Surface Temperature Retrieval From Landsat 8 Thermal Infrared Data Over Urban Areas Considering Geometry Effect: Method and Application. *IEEE Transactions on geoscience and remote sensing*.

Saputra, A.; M.H. Ibrahim; S. Shofirun; A. Saifuddin; and K. Furoida. 2022. Assessing urban heat island in Jakarta, Indonesia during the COVID-19 pandemic. In *IOP Conference Series: Earth and Environmental Science*, 012069: IOP Publishing.

Sarli, R. & G. Marapao. (2027). Global patterns and robustness of multi-indicator heat–drought climatic exposure across forest and cropland ecosystems under CMIP6 projections. *Global and Planetary Change* **268**:105810. https://doi.org/10.1016/j.gloplacha.2026.105810.

Sarli, R.; G. Marapao; A. Imam; E. Boldbaatar; and M. Alamoudi. 2026. Spatio-temporal assessment of urban vegetation cooling efficiency and the identification of critical heat mitigation zones in Kraków, Poland. *Progress in Physical Geography: Earth and Environment*. Advance online publication. https://doi.org/10.1177/03091333261466969.

Sarli, R.; V. Nasiri; P. Hawryło; and J. Socha. 2025. Evaluating the accuracy of the global precipitation products: a time-series analysis in Poland. *Climate Dynamics* **63**:155. https://doi.org/10.1007/s00382-025-07636-5.

Schaefer, M.; H.E. Salari; H. Köckler; and N.X. Thinh. 2021. Assessing local heat stress and air quality with the use of remote sensing and pedestrian perception in urban microclimate simulations. *Science of The Total Environment* **794:148709**.

Schwarz, N.; Lautenbach, S.; and Seppelt, R. 2011. Exploring indicators for quantifying surface urban heat islands of European cities with MODIS land surface temperatures. *Remote Sensing of Environment* **115:3175-3186**.

Sekertekin, A.; N. Arslan; and M. Bilgili. 2020. Modeling diurnal Land Surface Temperature on a local scale in an arid environment using an artificial Neural Network (ANN) and time series of Landsat-8-derived spectral indices. *Journal of Atmospheric and Solar-Terrestrial Physics* **206:105328**.

Shi, P.; Y. Dong; H. Yan; C. Zhao; X. Li; W. Liu; M. He; S. Tang; and S. Xi. 2020. Impact of temperature on the dynamics of the COVID-19 outbreak in China. *Science of The Total Environment* **728:138890**.

Snyder, W.C.; Z. Wan; Y. Zhang; and Y.-Z. Feng. 1998. Classification-based emissivity for land surface temperature measurement from space. *International Journal of Remote Sensing* **19:2753-2774**.

Srivastava, P.; T. Majumdar; and A.K. Bhattacharya. 2009. Surface temperature estimation in Singhbhum Shear Zone of India using Landsat-7 ETM+ thermal infrared data. *Advances in Space Research* **43:1563-1574**.

Tardy, B.; V. Rivalland; M. Huc; O. Hagolle; S. Marcq; and G. Boulet. 2016. A software tool for atmospheric correction and surface temperature estimation of Landsat infrared thermal data. *Remote Sensing* **8:696**.

Teufel, B.; L. Sushama; V. Poitras; T. Dukhan; S. Bélair; L. Miranda-Moreno; L. Sun; A.P. Sasmito; and G. Bitsuamlak. 2021. Impact of COVID-19-related traffic slowdown on urban heat characteristics. *Atmosphere* **12:243**.

Tobías, A.; Carnerero, C.; Reche, C.; Massagué, J.; Via, M.; Minguillón, M.C.; Alastuey, A.; and Querol, X. 2020. Changes in air quality during the lockdown in Barcelona (Spain) one month into the SARS-CoV-2 epidemic. *Science of The Total Environment* **726:138540**.

Valor, E. and V. Caselles. 1996. Mapping land surface emissivity from NDVI: Application to European, African, and South American areas. *Remote Sensing of Environment* **57:167-184**.

Venter, Z.S.; K. Aunan; S. Chowdhury; and J. Lelieveld. 2020. COVID-19 lockdowns cause global air pollution declines. *Proceedings of the National Academy of Sciences* **117:18984-18990**.

Wang, Q. & M. Su. (2020). A preliminary assessment of the impact of COVID-19 on the environment–A case study of China. *Science of The Total Environment* **728:138915**.

Weng, Q.; D. Lu; and J. Schubring. 2004. Estimation of land surface temperature–vegetation abundance relationship for urban heat island studies. *Remote Sensing of Environment* **89:467-483**.

Windahl, E. & K. de Beurs. (2016). An intercomparison of Landsat land surface temperature retrieval methods under variable atmospheric conditions using in situ skin temperature. *International journal of applied Earth observation and Geoinformation* **51:11-27**.

Yu, X.; X. Guo; and Z. Wu. 2014. Land surface temperature retrieval from Landsat 8 TIRS—Comparison between radiative transfer equation-based method, split window algorithm and single channel method. *Remote Sensing* **6:9829-9852**.

Yuan, F. & M.E. Bauer. (2007). Comparison of impervious surface area and normalized difference vegetation index as indicators of surface urban heat island effects in Landsat imagery. *Remote Sensing of Environment* **106:375-386**.

Yunus, A.P.; Y. Masago; and Y. Hijioka. 2020. COVID-19 and surface water quality: improved lake water quality during the lockdown. *Science of The Total Environment* **731:139012**.